Check for updates

ADVANCED MATERIALS
www.advmat.de

Printed High-Entropy Prussian Blue Analogs for Advanced Non-Volatile Memristive Devices

Yueyue He, Yin-Ying Ting, Hongrong Hu, Thomas Diemant, Yuting Dai, Jing Lin, Simon Schweidler, Gabriel Cadilha Marques, Horst Hahn, Yanjiao Ma, Torsten Brezesinski, Piotr M. Kowalski, Ben Breitung, and Jasmin Aghassi-Hagmann**

Non-volatile memristors dynamically switch between high (HRS) and low resistance states (LRS) in response to electrical stimuli, essential for electronic memories, neuromorphic computing, and artificial intelligence. High-entropy Prussian blue analogs (HE-PBAs) are promising insertion-type battery materials due to their diverse composition, high structural integrity, and favorable ionic conductivity. This work proposes a non-volatile, bipolar memristor based on HE-PBA. The device, featuring an active layer of HE-PBA sandwiched between Ag and ITO electrodes, is fabricated by inkjet printing and microplotting. The conduction mechanism of the Ag/HE-PBA/ITO device is systematically investigated. The results indicate that the transition between HRS and LRS is driven by an insulating-metallic transition, triggered by extraction/insertion of highly mobile Na^+ ions upon application of an electric field. The memristor operates through a low-energy process akin to Na^+ shuttling in Na-ion batteries rather than depending on formation/rupture of Ag filaments. Notably, it showcases promising characteristics, including non-volatility, self-compliance, and forming-free behavior, and further exhibits low operation voltage ($V_{SET} = -0.26$ V, $V_{RESET} = 0.36$ V), low power consumption ($P_{SET} = 26$ μW, $P_{RESET} = 8.0$ μW), and a high R_{OFF}/R_{ON} ratio of 10^4. This underscores the potential of high-entropy insertion materials for developing printed memristors with distinct operation mechanisms.

1. Introduction

The current Big Data era, driven by artificial intelligence and Internet of Things, demands processing exponentially increasing amounts of data, sparking tremendous interest in exploring emerging non-volatile memory technologies.[1–3] Such non-volatile memories are represented by devices known as memristors, which facilitate resistive switching (RS) between high (HRS) and low resistance states (LRS).[4] This capability enables efficient information processing for applications such as computation, data storage, and vision sensors.[5,6] Another benefit of non-volatile memristors is their ability to retain data during sudden power loss, like many state-of-the-art computing memory technologies, improving data safety.[2]

Conventional computing systems are constrained by the “von Neumann bottleneck”, where memory and processing units remain separate in digital hardware; memristors aspire to break through such

Y. He, H. Hu, Y. Dai, J. Lin, S. Schweidler, G. C. Marques, H. Hahn, T. Brezesinski, B. Breitung, J. Aghassi-Hagmann
Institute of Nanotechnology (INT)
Karlsruhe Institute of Technology (KIT)
Kaiserstr. 12, 76131 Karlsruhe, Germany
E-mail: ben.breitung@kit.edu; jasmin.aghassi@kit.edu

Y.-Y. Ting, P. M. Kowalski
Institute of Energy Technologies (IET-3)
Forschungszentrum Jülich GmbH
Wilhelm-Johnen-Str., 52428 Jülich, Germany

The ORCID identification number(s) for the author(s) of this article can be found under https://doi.org/10.1002/adma.202410060

© 2024 The Author(s). Advanced Materials published by Wiley-VCH GmbH. This is an open access article under the terms of the Creative Commons Attribution-NonCommercial License, which permits use, distribution and reproduction in any medium, provided the original work is properly cited and is not used for commercial purposes.

DOI: 10.1002/adma.202410060

Y.-Y. Ting
Chair of Theory and Computation of Energy Materials
Faculty of Georesources and Materials Engineering
RWTH Aachen University
52062 Aachen, Germany

Y.-Y. Ting, P. M. Kowalski
Jülich Aachen Research Alliance
JARA Energy & Center for Simulation and Data Science (CSD)
52428 Jülich, Germany

T. Diemant
Helmholtz Institute Ulm (HIU) for Electrochemical Energy Storage
Helmholtzstr. 11, 89081 Ulm, Germany

Y. Dai
Department of Materials and Earth Sciences
Technical University Darmstadt
64287 Darmstadt, Germany

limitations.[7] Due to their appealing characteristics such as fast switching speed, high scalability, and ease of fabrication,[8] memristors offer many possibilities for the rapid development of computing architectures, particularly in neuromorphic and in-memory computing systems.[9,10] To date, a wide range of materials demonstrating versatile applicability for memristors, including metal oxides,[11–13] chalcogenides,[14] 2D materials,[15,16] molecular materials,[17] hybrid perovskites,[18,19] organic materials,[20] silicon,[21,22] nitrides,[23,24] and carbonaceous materials,[25] have garnered considerable attention. Nevertheless, to the best of our knowledge, only few studies have explored insertion materials as potential RS candidates,[26] and there is a lack of investigations into high-entropy materials (HEMs).

The high-entropy concept delineates a strategic approach involving the incorporation of five or more elements into a unified phase structure, leveraging their interactions to produce synergistic effects, commonly referred to as cocktail effects.[27–29] HEMs are characterized as compounds featuring a minimum of five distinct elements, with atomic ratios ranging between 5 and 35 at.%.[29] Alternatively, they can be defined as materials with a configurational entropy exceeding 1.5R, where R represents the ideal gas constant. HEMs present noteworthy capabilities for compositional and functional tunability, wherein elements can be systematically replaced, added, or removed.[28] These modifications inherently lead to altered interactions, thus influencing the material properties. HEMs feature applications mainly involving thermoelectrics,[30,31] catalysis,[32–34] environmental protection, and energy storage.[28,35] As an example, the burgeoning applications of high-entropy insertion materials in the realm of rechargeable batteries[35–38] stem from their ability to stabilize reversible insertion/extraction of ions into/from the lattice without altering the original crystal structure.

Prussian blue analogs (PBAs), a prominent family of metal–organic frameworks (MOFs), exhibit a rigid 3D open framework with large interstitial sites conducive to high mobility of Na^+. Characterized by the general formula $Na_xM[Fe(CN)_6]_y\square_{1-y}\cdot nH_2O$ (where $0 < x \leq 2$, $0 < y \leq 1$, M represents transition-metal ions, $\square$ signifies $[Fe(CN)_6]$ vacancies, and n is interstitial water content in the crystal framework),[39,40] they offer the flexibility to tailor the M position, and with that also the composition and properties using the high-entropy approach. High-entropy PBAs (HE-PBAs) have been demonstrated to be robust (virtually zero-strain) host materials for sodium-ion batteries (SIBs)[35–37] and exhibit great potential in electrochemical energy storage.[28,41] These attributes directly lend themselves to the design of new insertion-type memristors, characterized by excellent reproducibility and controllability owing to robust ion diffusion that can be reversibly controlled by the applied bias voltage. Given these advantageous characteristics, high Na^+ diffusion coefficient (≈10^{-9} cm^2 s^{-1}),[42,43] stable structure, and favorable ionic conductivity,[44] HE-PBAs confer high flexibility in designing memristive devices with superior performance. However, the application of HE-PBAs as insertion materials in memristors is still underexplored, and their resistive switching mechanisms are not well understood.

In this study, we present a promising non-volatile, bipolar memristor based on HE-PBA modulated by Na^+ ions. The device consists of a microplotted HE-PBA active layer, specifically $Na_{1.38}Mn_{0.3}Fe_{0.3}Co_{0.133}Ni_{0.133}Cu_{0.133}[Fe(CN)_6]_{0.84}\square_{0.16}\cdot 0.92H_2O$, with a laser-ablated indium tin oxide (ITO) bottom electrode (BE) and an inkjet-printed Ag top electrode (TE). The Ag/HE-PBA/ITO device exhibits low power consumption, self-compliance, and a forming-free nature. The underlying resistive switching mechanism of the memristor was thoroughly investigated through complementary characterizations and density functional theory (DFT) calculations. The resistive changes were effectively controlled by fast sodium migration under an electric field, resulting in a Na^+-deficient layer of high conductivity with metallic conduction behavior. Furthermore, this work focuses on fabricating memristors using printed technologies, including inkjet printing and microplotting. These methods allow for precise, low-cost, and on-demand fabrication of a large number of electronic devices.[45,46] By contrast, other advanced manufacturing methods like atomic layer deposition,[47] spin coating,[48] sputtering,[49] pulsed laser deposition, or photolithographic techniques[21,50] are inherently complex and costly. Therefore, the exploration of printed memristors merits further in-depth study. As a result, the printed Ag/HE-PBA/ITO device demonstrates several advantages for memristor applications, including low operation voltage, good retention stability, and a high R_{OFF}/R_{ON} ratio. These characteristics position it as a promising candidate for non-volatile memory applications with low power consumption.

2. Results and Discussion

2.1. Printing of HE-PBA Memristor

The printed HE-PBA-based memristor was structured as shown in **Figure 1a**. A commercial ITO electrode was patterned using laser ablation on ITO-coated glass substrates, serving as BE. A subsequent plasma treatment was conducted to optimize the surface hydrophilicity, resulting in a significantly reduced water contact angle, as shown in Figure S1 (Supporting Information). This treatment ensured optimal conditions for the subsequent deposition of the ink. The latter ink was composed of pre-synthesized HE-PBA powder dispersed in a mixture of deionized water (97% vol.) and dimethyl sulfoxide (DMSO, 3% vol.) to reduce the "coffee ring" effect during printing (Figure S2, Supporting Information). In comparison to aqueous inks, DMSO with its higher boiling point, lower evaporation rate, and greater viscosity, slows the drying process, reducing particle migration and promoting a more uniform particle distribution across the substrate. This helps to prevent the formation of ring-like deposits, ensuring a more homogeneous printed layer. The HE-PBA ink was printed onto the ITO electrode by microplotting, using the "U"-shaped

H. Hahn
School of Chemical
Biological and Materials Engineering
The University of Oklahoma
Norman, OK 73019, USA
Y. Ma
School of Energy and Mechanical Engineering
Jiangsu Key Laboratory of New Power Batteries
Nanjing Normal University
Nanjing 210023, China

© 2024 The Author(s). Advanced Materials published by Wiley-VCH GmbH

15214095, 0, Downloaded from https://onlinelibrary.wiley.com/doi/10.1002/adma.202410060 by Karlsruher Institut F., Wiley Online Library on [08/12/2024]. See the Terms and Conditions (https://onlinelibrary.wiley.com/terms-and-conditions) on Wiley Online Library for rules of use; OA articles are governed by the applicable Creative Commons License

15214095, 0, Downloaded from https://onlinelibrary.wiley.com/doi/10.1002/adma.202410060 by Karlsruher Institut F., Wiley Online Library on [08/12/2024]. See the Terms and Conditions (https://onlinelibrary.wiley.com/terms-and-conditions) on Wiley Online Library for rules of use; OA articles are governed by the applicable Creative Commons License

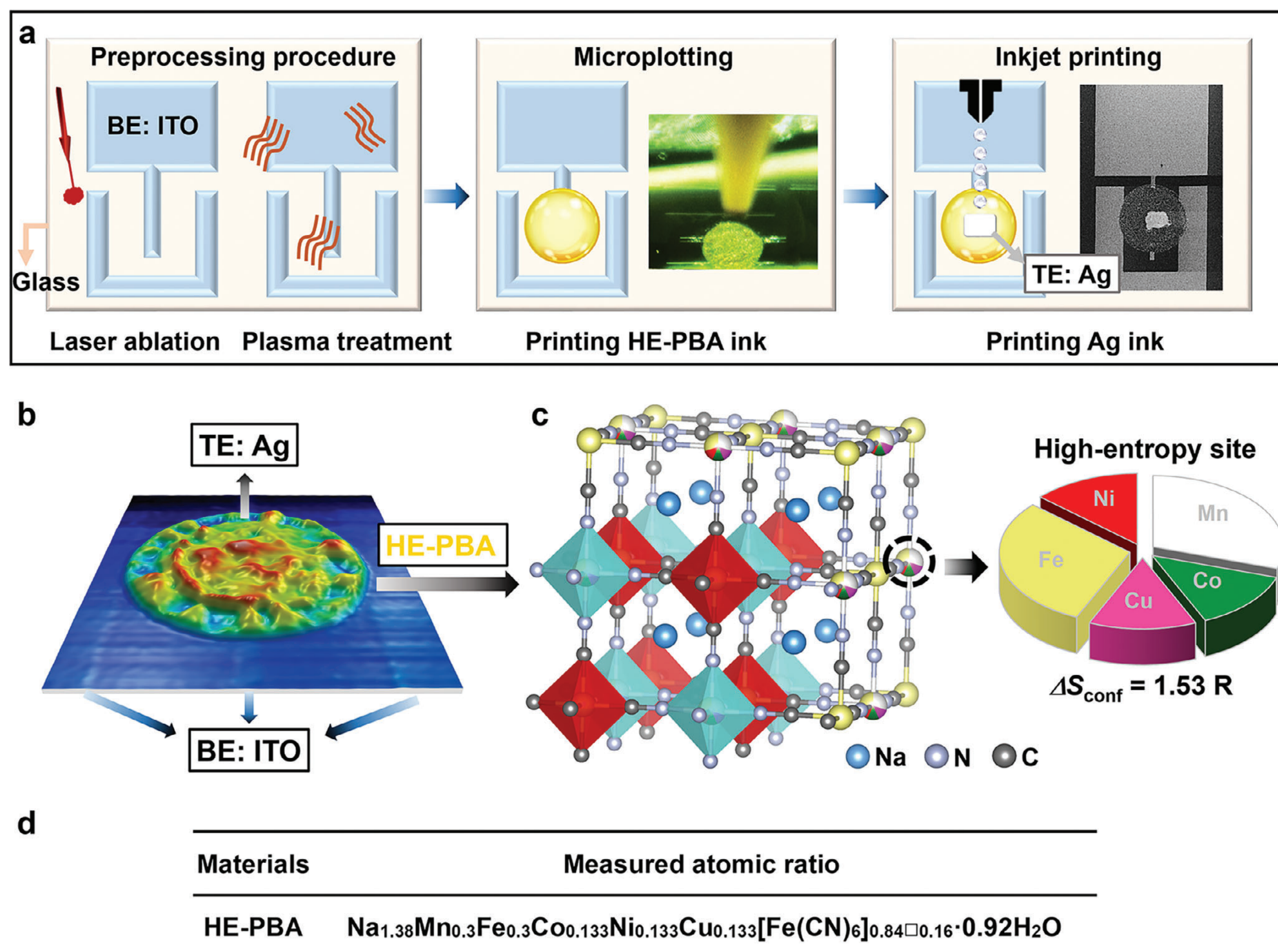

Materials	Measured atomic ratio
HE-PBA	$Na_{1.38}Mn_{0.3}Fe_{0.3}Co_{0.133}Ni_{0.133}Cu_{0.133}[Fe(CN)_6]_{0.84}\square_{0.16}\cdot 0.92H_2O$

Figure 1. a) Schematics of the device fabrication process. b) 3D top view of the Ag/HE-PBA/ITO memristor. c) Crystal structure of HE-PBA from Rietveld refinement analysis and d) composition of the multi-elemental site from ICP-OES and DSC.

structure as positioning reference (Figure 1a). Finally, a commercially available Ag ink was inkjet-printed as TE onto the HE-PBA layer. Detailed fabrication steps can be found in the experimental section of the Supporting Information. A 3D topography of the printed device is shown in Figure 1b, illustrating the architecture of the three stacked layers. The TE made of Ag was inkjet-printed, which results in the heightened area in the middle (depicted in red) of the lower round area (depicted in blue/green), representing the HE-PBA layer. Regarding the BE, the patterned ITO lies below the printed materials and can be seen at the sides as indicated.

Earlier studies on HE-PBAs reported a local structure that shows Fe_1 atoms at the C-coordinated 4*a* sites of the PBA lattice ($Na_xM[Fe_1(CN)_6]$), while the other metal atoms M (M = Mn, Fe_2, Co, Ni, and Cu) occupy the N-coordinated 4*b* positions in a random fashion, leading to the formation of linear chains of $Fe_1-C\equiv N-Mn/Fe_2/Co/Ni/Cu-N\equiv C-Fe_1$ along the cube edges,[35–37] as illustrated in Figure 1c. Inductively coupled plasma-optical emission spectroscopy (ICP-OES) was used to analyze the chemical composition of the HE-PBA, and differential scanning calorimetry (DSC; Figure S3, Supporting Information) was conducted to estimate the content of crystal water in the sample. As shown in Figure 1d, the chemical formula was determined to be $Na_{1.38}Mn_{0.3}Fe_{0.3}Co_{0.133}Ni_{0.133}Cu_{0.133}[Fe(CN)_6]_{0.84}\square_{0.16}\cdot 0.92H_2O$. Murty et al.[51] suggested an empirical classification for such materials based on the configurational entropy (ΔS_{conf}), which can be calculated by statistical thermodynamics (see Equations S1 and S2, Supporting Information). Here, the ΔS_{conf} of HE-PBA is 1.53*R*, which categorizes the compound as a HEM.

The active material was characterized before and after ink preparation to ensure its purity and stability in the dispersant. X-ray diffraction (XRD) was performed to analyze the structure of HE-PBA. **Figure 2a** shows reflections corresponding to the (200), (220), (400), (420), and (422) crystal planes, which align well with a face-centered cubic structure (space group: *Fm*−3*m*, ICSD coll. code 193354),[52] as previously reported in the literature for PBA compounds.[39] No differences in the patterns can be observed between pristine HE-PBA and the material dispersed in the ink. Notably, the crystal structure remained stable even after the ink had been stored for almost four months (Figure 2a), indicating high ink stability. In addition, selected-area electron diffraction

 © 2024 The Author(s). Advanced Materials published by Wiley-VCH GmbH

15214095, 0, Downloaded from https://onlinelibrary.wiley.com/doi/10.1002/adma.202410060 by Karlsruher Institut F., Wiley Online Library on [08/12/2024]. See the Terms and Conditions (https://onlinelibrary.wiley.com/terms-and-conditions) on Wiley Online Library for rules of use; OA articles are governed by the applicable Creative Commons License

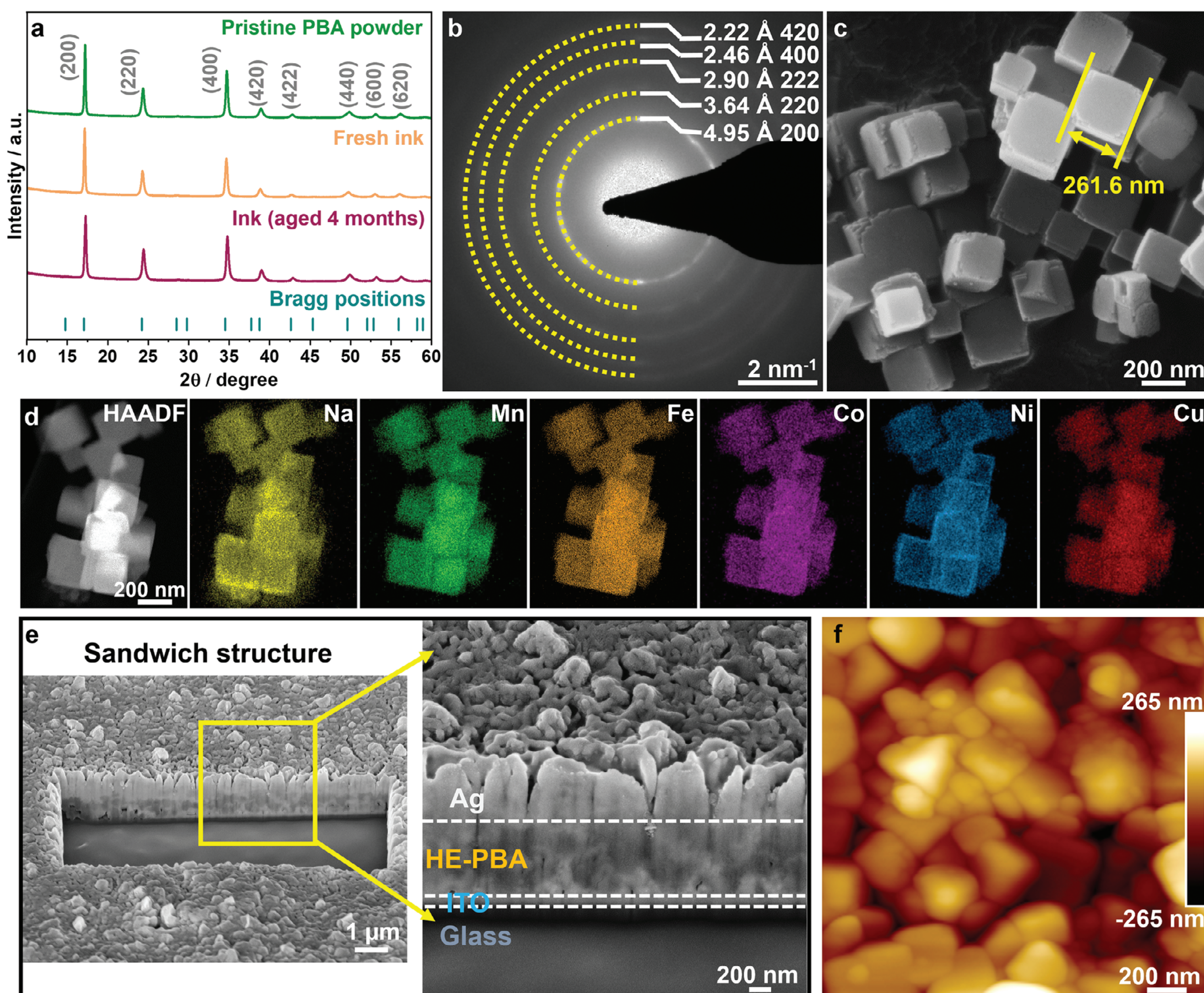

Figure 2. Structural and morphological characteristics of the HE-PBA. a) XRD pattern, b) SAED pattern, c) SEM image, and d) STEM-EDS elemental mapping results. e) Cross-sectional SEM image of the device structure, showing three layers of materials, namely Ag, HE-PBA, and ITO. f) Surface analysis of the HE-PBA film via AFM.

(SAED) was performed to further confirm the crystal structure (Figure 2b). The diffraction rings with *d*-spacings of 4.95, 3.64, 2.90, 2.46, and 2.22 Å can be associated with the (200), (220), (222), (400), and (420) planes of the cubic HE-PBA structure. The results are in agreement with the XRD findings, confirming the absence of secondary phases in the sample. Scanning electron microscopy (SEM, Figure 2c) shows that the HE-PBA particles are cubic in shape with average dimensions of 200–300 nm. High-angle annular dark-field scanning transmission electron microscopy (HAADF-STEM) imaging, combined with energy-dispersive X-ray spectroscopy (EDS) mapping (Figure 2d), confirmed the presence of Na, Mn, Fe, Co, Cu, and Ni at the given resolution. Some slight Ni enrichment at the grain boundaries was observed, likely due to diffusion and/or surface energy effects during the formation of material. The proportions of each element in HE-PBA obtained by STEM-EDS analysis (Table S1, Supporting Information) are consistent with the ICP-OES results. Additionally, the printed memristor was characterized to confirm successful structuring. A focused ion beam (FIB) cut of the printed memristor (Figure 2e) was prepared, showing a sandwich structure with ≈800 nm thickness of the HE-PBA layer. The effective area of the Ag/HE-PBA/ITO device, determined by the overlap between BE and TE, was calculated to be ≈30 × 120 μm^2. The surface of the HE-PBA film was further probed using atomic force microscopy (AFM). As shown in Figure 2f, the surface has a relatively large root mean square roughness (R_q) of ≈70 nm, simply because the HE-PBA film is made up of an array of cubic particles in a disordered manner. Micro X-ray fluorescence (μXRF; Figure S4, Supporting Information) measurements confirmed the presence of the aforementioned elements in the active layer and indicated that no changes in elemental composition occur during device fabrication.

Fourier transform infrared (FT-IR) spectroscopy was performed to further examine the structure of HE-PBA. **Figure 3a**

 © 2024 The Author(s). Advanced Materials published by Wiley-VCH GmbH

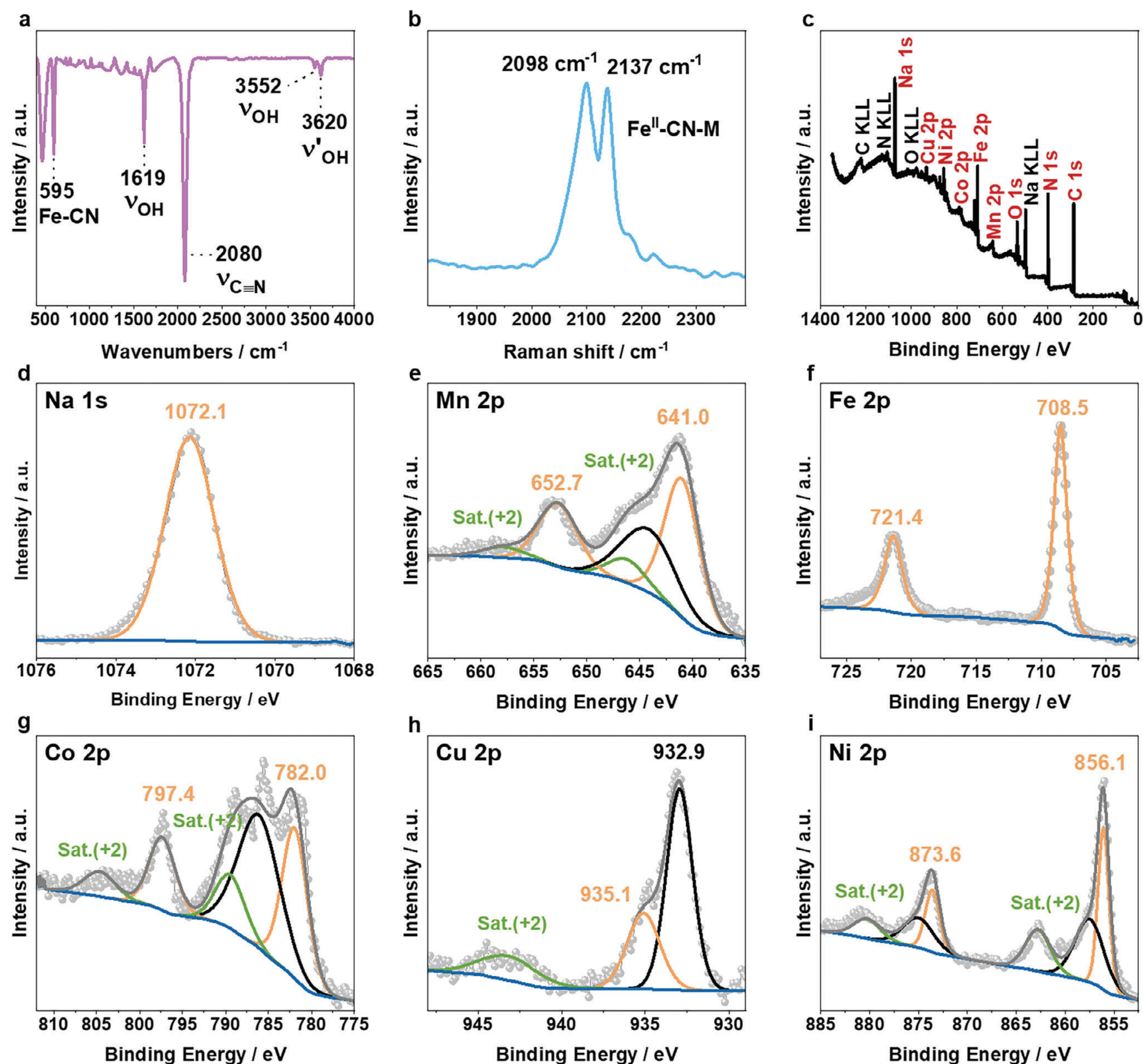

Figure 3. Structural characterization and surface chemical state of the HE-PBA. a) FT-IR spectrum. b) Raman spectrum. c) XPS survey spectrum and detail spectra of the d) Na 1s, e) Mn 2p, f) Fe 2p, g) Co 2p, h) Cu 2p, and i) Ni 2p regions.

shows absorption bands at 1619 and 3552 cm^{-1}, corresponding to O-H stretching and H-O-H bending, respectively, corroborating the presence of crystal water in the material.[53] The pronounced broad peak at ≈2080 cm^{-1} can be attributed to the stretching vibration from C≡N, and the sharp peak in the low wavenumber region at 595 cm^{-1} is closely related to the Fe-CN vibration.[54] In addition, Raman spectroscopy was used to investigate the interactions between the cyanide and transition-metal ions, since the frequency of the ν(CN) cyanide stretching vibration mode is very sensitive to the oxidation state of iron and its surrounding coordination environment.[55–57] As shown in Figure 3b, two strong bands appeared at ≈2098 and 2137 cm^{-1}, which can be assigned to Fe^{2+}-CN-M, similar to the ν(CN) bands of $K_4[Fe(CN)_6]$ reported by Samain et al.[56] In contrast, peaks at higher wavenumbers are expected for the stretching vibration of $[Fe(CN)_6]^{3-}$.[55,56]

X-ray photoelectron spectroscopy (XPS) measurements were conducted to investigate the surface chemical state of HE-PBA. The survey spectrum displayed in Figure 3c confirms the presence of the expected elements (C, N, Na, Mn, Fe, Co, Cu, and Ni). In the Na 1s spectrum (Figure 3d), a single peak at 1072.1 eV was detected corresponding to the Na^+ ions in the lattice. The Mn 2p spectrum (Figure 3e) exhibits a primary peak doublet at 641.0 eV ($2p_{3/2}$) and 652.7 eV ($2p_{1/2}$), together with distinct satellite peaks at 646.2/657.9 eV and a broad Ni Auger line at ≈644 eV. The binding energy of the main peak doublet and the presence of shake-up satellites point to an oxidation state of +2 for Mn.[37,58]

© 2024 The Author(s). Advanced Materials published by Wiley-VCH GmbH

15214095, 0, Downloaded from https://onlinelibrary.wiley.com/doi/10.1002/adma.202410060 by Karlsruher Institut F., Wiley Online Library on [08/12/2024]. See the Terms and Conditions (https://onlinelibrary.wiley.com/terms-and-conditions) on Wiley Online Library for rules of use; OA articles are governed by the applicable Creative Commons License

ADVANCED MATERIALS
www.advmat.de

The Fe 2p spectrum (Figure 3f) shows a single peak doublet at 708.5 and 721.4 eV; these binding energies are typical of Fe^{2+} in the $[Fe(CN)_6]^{4-}$ unit (or other Fe^{2+} compounds).[36,53,59,60] The absence of additional features suggests that the iron coordinated to nitrogen is also in the +2 oxidation state. Figure 3g shows the Co 2p spectrum, which is constituted by the main Co 2p peak doublet (782.0/797.4 eV) and pronounced shake-up satellites (789.5/804.7 eV), together with a broad Fe Auger feature at ≈786 eV. Since these satellite peaks are characteristic of Co^{2+}, it is inferred that Co is present in the 2+ oxidation state.[36,37] The major peak in the Cu 2p spectrum (Figure 3h) at 932.9 eV (Cu $2p_{3/2}$) can be assigned to Cu^+.[37] Additionally, another peak is detected at a higher binding energy (935.1 eV), and its corresponding shake-up satellite at ≈943 eV can be ascribed to the presence of Cu^{2+}.[61,62] The detection of Cu^+ implies that an internal redox reaction, involving the reduction of Cu^{2+} to Cu^+, occurred during synthesis—a process previously observed in earlier studies.[35,38] Finally, the Ni 2p spectrum (Figure 3i) shows major peaks at 856.1 eV (Ni $2p_{3/2}$) and 873.6 eV (Ni $2p_{1/2}$), accompanied by another doublet at slightly higher binding energies of 857.6 and 875.1 eV as well as satellite peaks at 862.8 and 880.3 eV.[36] The complex peak splitting makes it complicated to unequivocally determine the Ni oxidation state; because the Ni $2p_{3/2}$ peak of NiO appears at ≈854 eV and that of $Ni(OH)_2$ is detected at ≈856 eV, close to the binding energy of Ni_2O_3.[63] However, prior results from normalized *K*-edge X-ray absorption near edge spectroscopy suggest an oxidation state of +2.[35,36] Hence, the initial average oxidation state of both Fe_1 binding to the carbon atoms and M (Mn, Fe_2, Co, Cu, and Ni) binding to the nitrogen atoms of the $C{\equiv}N^-$ ligands is determined to be +2, as expected for the PBA structure with linear chains of $Fe_1{-}C{\equiv}N{-}Mn/Fe_2/Co/Ni/Cu{-}N{\equiv}C{-}Fe_1$.

2.2. Electrical Properties

The RS behavior of the Ag/HE-PBA/ITO device was analyzed by current–voltage (*I*–*V*) characterization. Figure S5 (Supporting Information) shows the *I*–*V* curves for all 800 sweeping cycles while **Figure** 4a focuses on selected *I*–*V* profiles plotted on a semilogarithmic scale. All voltage sweeps were performed at a fixed rate of 0.01 V per step. The bias voltage was applied to the Ag TE with the ITO electrode grounded. As displayed in Figure 4a, the as-fabricated Ag/HE-PBA/ITO device exhibits a typical bipolar RS behavior.[5,13] When a negative voltage sweep (0 V → -0.4 V → 0 V) was applied, the device in a HRS of 2.6×10^7 Ω (OFF state) could be "SET" to a LRS (ON state, 5.3×10^3 Ω for the first cycle). This transition from HRS to LRS is equiv. to a "writing" process in data-storage devices.[64] In contrast, during a positive voltage sweep (0 V → 0.9 V → 0 V), a drastic drop in current at ≈0.5 V indicates reversal of the effect (see green line in Figure 4a) that restored the device back to a HRS (2.5×10^6 Ω), which is commonly referred to as "RESET" process. This shift from LRS to HRS corresponds to an "erasing" process in digital memory devices.[64,65] The voltage at which the RS occurs during the SET and RESET process is denoted as V_{SET} and V_{RESET}, respectively. With increasing voltage, the LRS current increased slightly and showed a low self-compliance of 44.3 μA when exceeding the V_{SET} in the SET process. This feature highlights a significant advantage of the device, as a current limitation is usually required to prevent dielectric breakdown from high currents.[66] However, the present device demonstrates self-limitation, known as self-compliance, which allows it to operate without the need for an external compliance current (CC).[47,67] Moreover, the memristor can be cycled consecutively over 800 times, showing reversible bipolar RS behavior, as well as stable self-compliance character, as shown in Figure S5 (Supporting Information).

The corresponding V_{SET} and V_{RESET} values from the 800 write and erase cycles were extracted and plotted in a histogram in Figure 4b. A narrow distribution between −0.33 to −0.22 V was observed for V_{SET}, while V_{RESET} varied between 0.02 and 0.4 V, with minor outliers up to 0.9 V. The inserted box plots yield mean values for V_{SET} and V_{RESET} of −0.26 and 0.36 V, respectively, which are much lower than that of other reported insertion materials (Table S2, Supporting Information).[68,69] The standard deviation (σ) with distribution width of 0.02 V for V_{SET} suggests a small cycle-to-cycle variability. Typically, the initial electroforming process requires a higher voltage than subsequent SET processes to induce the formation of a conductive path (e.g., conducting filament) at the beginning.[13,65] However, in the case of Ag/HE-PBA/ITO device, an excellent consistency in switching voltage is found right from the start, indicating a forming-free mechanism. Figure S6 (Supporting Information) illustrates SET and RESET power data defined by the product of switching current and voltage.[70,71] The device demonstrates low power consumption during the SET process (P_{SET}), ranging from 20.6 to 36.9 μW, with an average of 26.1 μW. For the RESET process (P_{RESET}), the power averages 8.0 μW, slightly extending up to 104.7 μW. This is considerably lower than that of other reported devices with self-compliance behavior,[47,67,72] as summarized in Table S3 (Supporting Information). The endurance of the Ag/HE-PBA/ITO device, demonstrated by the ratio of HRS and LRS values over cycling, is plotted in Figure 4c. The R_{OFF}/R_{ON} ratio remains close to 10^4, with further clarification provided by the corresponding cumulative probability data in Figure S7 (Supporting Information). It is worth noting that there is no obvious degradation after 800 switching cycles. The variation in conductivity observed in Figure 4c will be discussed in more detail below (see section on resistive switching mechanism). Notably, the device features excellent retention characteristics (see Figure 4d), maintaining a stable R_{OFF}/R_{ON} ratio of 10^4 over 4×10^4 s (≈10^7 Ω for HRS and 10^3 Ω for LRS), indicating significant potential for non-volatile memory applications in digital information storage.[2,73] Comparing the performance of HE-PBA with previously reported conventional PBAs (single-metal, $\Delta S_{conf} = 0R$) used as storage layer in memristors (Table S4, Supporting Information)[54,74,75] highlights the significant improvement in endurance and retention capability achieved with the Ag/HE-PBA/ITO device. This result underscores the positive effect that an increased ΔS_{conf} may have on the performance of memristors.

In addition, *I*–*V* data were collected on five different devices to investigate the device-to-device uniformity. As shown in Figure S8 (Supporting Information), the bipolar RS behavior with self-compliance characteristics is visible for all devices. Detailed box plots of the extracted V_{SET} and V_{RESET} for each device are displayed in Figure 4e while Figure S9 (Supporting Information) shows the corresponding mean values of V_{SET} and V_{RESET}. D2, D3, D4, and D5 show a similar mean value for V_{SET} (below −0.14 V) while ≈−0.20 V is found for D1. The mean V_{RESET} values are

© 2024 The Author(s). Advanced Materials published by Wiley-VCH GmbH
15214095, 0, Downloaded from https://onlinelibrary.wiley.com/doi/10.1002/adma.202410060 by Karlsruher Institut F., Wiley Online Library on [08/12/2024]. See the Terms and Conditions (https://onlinelibrary.wiley.com/terms-and-conditions) on Wiley Online Library for rules of use; OA articles are governed by the applicable Creative Commons License

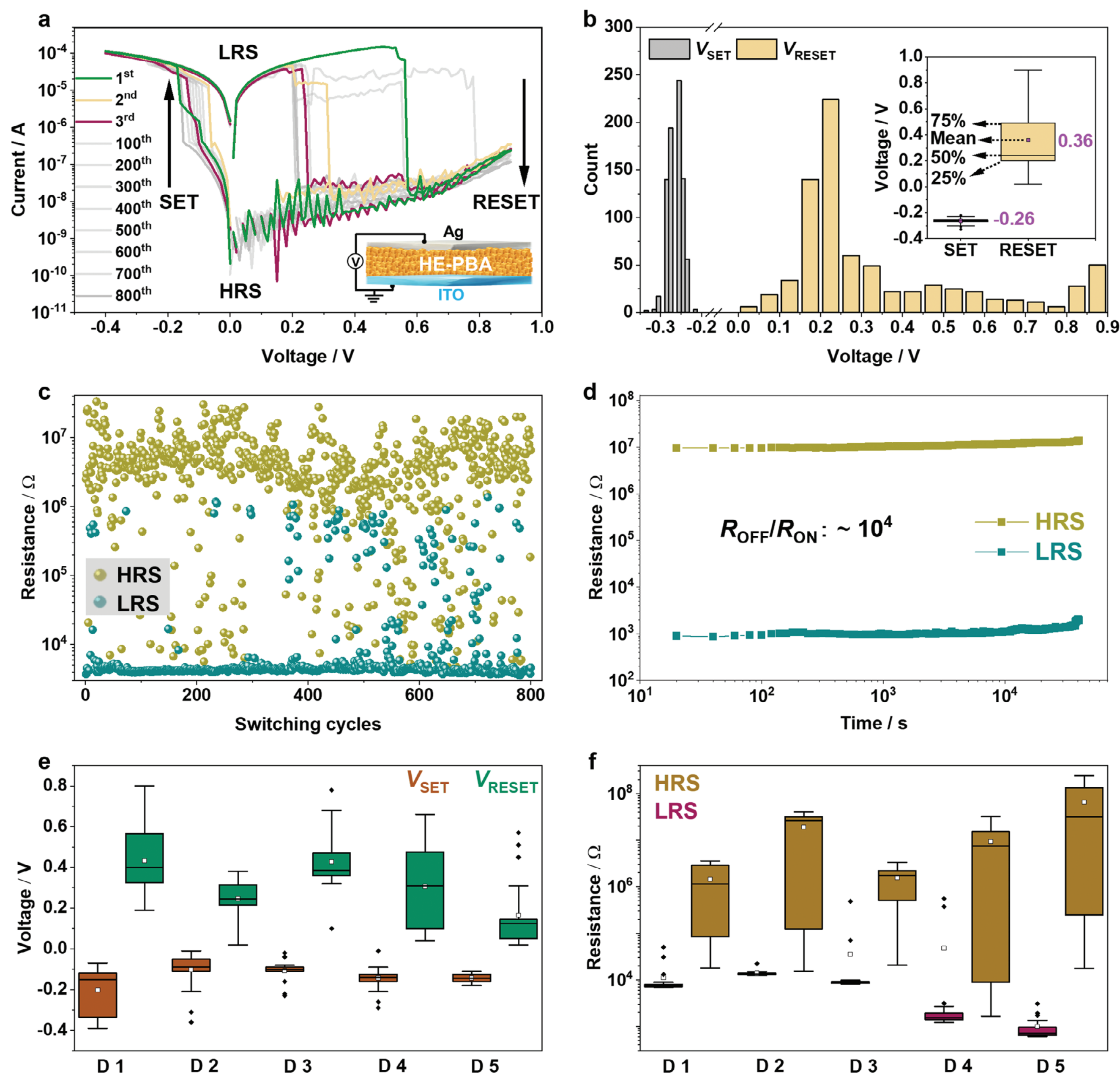

Figure 4. Electric characterization of the Ag/HE-PBA/ITO memristor. a) Selected *I–V* curves plotted on a semi-logarithmic scale (1st, 2nd, 3rd, 100th, 200th, 300th, 400th, 500th, 600th, 700th, and 800th). b) Distribution of V_{SET} and V_{RESET} extracted from the 800 consecutive *I–V* sweeps, with the inset showing the statistical analysis of V_{SET} and V_{RESET} using box plots. c) Endurance over 800 sweeping cycles. d) Retention at HRS and LRS over 4×10^4 s. e) Statistical analysis of V_{SET} and V_{RESET} from five different devices displayed in box plots. f) Box plots depicting the distribution of HRS and LRS across the five devices.

0.43, 0.25, 0.43, 0.31, and 0.17 V, respectively, for D1 to D5. The fluctuation of RESET process is below 0.9 V, which can be expected to get improved by optimizing the measurement procedure, along with implementing advanced feedback algorithms in the future.[76] The small variability of V_{SET} and V_{RESET} across different devices indicates that the HE-PBA-based memristors are fully capable of operating at very low SET and RESET voltages (as low-power memory devices). An R_{OFF}/R_{ON} ratio of more than 10^3 is observed for D2, D4, and D5 (Figure 4f). To further examine the dynamic RS behavior of the Ag/HE-PBA/ITO device for non-volatile memory application, pulsed operations were applied for SET and RESET over 500 cycles,[77] as illustrated in Figure S10 (Supporting Information). "Write" operation was achieved with a −0.4 V pulse, and "erase" operation with a 0.5 V pulse, both without CC. The pulse width for both operations was 0.2 s, with resistance measured using a 0.01 V read pulse of equal duration. The results demonstrate the good performance of the printed memristor, which can readily switch between HRS and

© 2024 The Author(s). Advanced Materials published by Wiley-VCH GmbH

15214095, 0, Downloaded from https://onlinelibrary.wiley.com/doi/10.1002/adma.202410060 by Karlsruher Institut F., Wiley Online Library on [08/12/2024]. See the Terms and Conditions (https://onlinelibrary.wiley.com/terms-and-conditions) on Wiley Online Library for rules of use; OA articles are governed by the applicable Creative Commons License

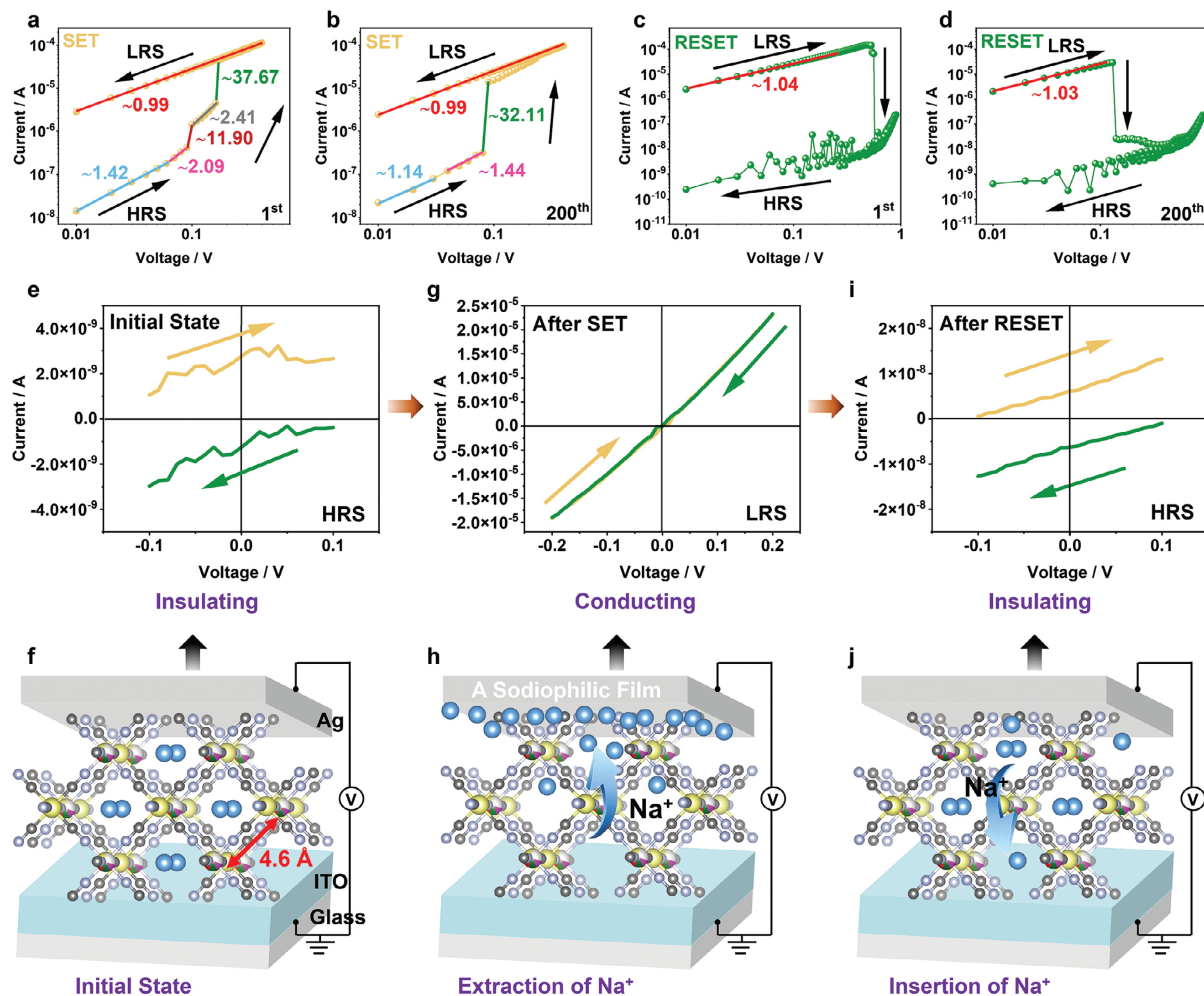

Figure 5. Analysis of the conduction mechanism. Double-logarithmic *I*–*V* curves for a,b) SET and c,d) RESET process. e,g,i) *I*–*V* measurements on a random device in the initial state, LRS, and HRS, respectively, with a maximum applied voltage well below V_{SET} and V_{RESET}. f,h,j) Corresponding schematic representations of the conduction mechanism.

LRS at low applied voltages and without CC over extended cycles. Some studies indicate that the use of insertion materials remains challenging, which is mainly reflected by their often unfavorable operation parameters, i.e., high voltage and current,[6,68] as displayed in Table S2 (Supporting Information). Compared to these devices, the properties of the Ag/HE-PBA/ITO memristor in terms of switching endurance, power consumption, and retention are superior, highlighting the advantage of HEMs for such devices.

2.3. Resistive Switching Mechanism

In the next step, we attempted to understand the conduction mechanism by linear fitting of selected double-logarithmic *I*–*V* curves based on the SET and RESET process. For the SET process (**Figure** 5a,b), after reaching the LRS of device, the linear fitting with a slope close to 1 reveals an ohmic conduction mechanism, which is in line with the study of Chiu et al.[78] For the RESET process, the high degree of noise present after linear reduction of the current in the OFF state (Figure 5c,d) renders it challenging to identify the conduction mechanism. Therefore, the resistive switching mechanism was further investigated by conducting *I*–*V* measurements in the initial state, LRS, and HRS, with the maximum applied voltage being well below V_{SET} and V_{RESET} to prevent resistive switching. The curved profiles delineating the evolution of current in the initial state and HRS (Figure 5e,i) were comparable, as neither crossed the origin. In contrast, after the SET process, the device exhibited a notable change, distinctly crossing the origin with a much higher slope, as shown in Figure 5g. The distinct *I*–*V* characteristics in the LRS point to a highly conductive nature of the device. The temperature dependence of the resistivity in the LRS (Figure S11, Supporting Information) also indicates a more "metallic" type of conduction, i.e.,

© 2024 The Author(s). Advanced Materials published by Wiley-VCH GmbH

15214095, 0, Downloaded from https://onlinelibrary.wiley.com/doi/10.1002/adma.202410060 by Karlsruher Institut F., Wiley Online Library on [08/12/2024]. See the Terms and Conditions (https://onlinelibrary.wiley.com/terms-and-conditions) on Wiley Online Library for rules of use; OA articles are governed by the applicable Creative Commons License

an increase in resistivity with increasing temperature. While for most metals a linear dependency of resistivity with temperature is observed, here we assume that the Ag/HE-PBA and ITO/HE-PBA contacts affect the behavior. Lee et al.[72] reported that an internal ohmic resistance can play a critical role with regard to self-compliance behavior, since such an internal resistance would limit the current flow in the LRS.[71]

To determine whether the self-compliance originates from the ITO or HE-PBA, commercial Au as BE was tested in place of ITO (Figure S12, Supporting Information). Laser ablation was employed to pattern the Au electrode, following the same procedure as for ITO. The results show that the self-compliance behavior is indeed due to the internal ohmic resistance of the HE-PBA, as self-compliance persists even without the use of ITO. Additionally, *I*–*V* measurements were conducted in the LRS, keeping the applied voltage well below V_{SET} to avoid triggering resistive switching. The resulting curve (Figure S12, Supporting Information) crosses the origin and shows a steeper slope, indicating lower resistivity and more metallic-like conduction, consistent with previous discussions. However, it was also observed that the self-compliance current in the Ag/HE-PBA/Au configuration is relatively large, and in some cases, an external CC is necessary to reduce power consumption and protect the device, especially in consecutive cycles. This suggests that the role of ITO in the self-compliance mechanism cannot be fully ruled out, likely due to higher conductivity of Au, which increases the need for a CC. Nevertheless, it remains clear that the internal ohmic resistance of the HE-PBA significantly contributes to the self-compliance behavior, particularly in the Ag/HE-PBA/ITO configuration.

Typically, internal ohmic conduction occurs due to movement of mobile electrons in the conduction band and holes in the valence band.[78] RS devices utilizing insertion materials often rely on ion-modulated electronic conductivity.[26,69] This is because the extraction/insertion of mobile ions induces (nearly) free electrons/holes in the conduction/valence bands.[79,80] To understand the working mechanism of the bipolar memristor (Ag/HE-PBA/ITO), it is essential to investigate the sodium transport processes within the device. In fact, the transport processes in PBA have been thoroughly studied and reported for advanced SIBs.[35,37,40] As illustrated in Figure 5f, the open 3D framework structure of HE-PBAs provides large interstitial sites (≈4.6 Å in diameter) that can accommodate alkali ions ($r_{\mathrm{Na^+}} \approx 1.0$ Å), as well as spacious channels,[39,40] enabling rapid solid-state diffusion of various carrier ions. It is expected that the application of a negative voltage to the Ag TE will drive positively charged Na^+ ions toward that electrode under the electric field (Figure 5h), leading to oxidation of low-valence metal ions (Mn^{2+}, Fe^{2+}, Co^{2+}, etc.) for maintaining charge neutrality.

Ag-based electrodes have been intensely investigated for rechargeable lithium or sodium batteries due to their high conductivity, good mechanical flexibility, and intrinsic lithiophilic/sodiophilic nature.[81–83] We assume that similar properties are fundamentally important for driving the resistive switching mechanism. The possible interactions between Na^+ and Ag differ from those between Na^+ and ITO, and most likely support the stability of the respective state. On the one hand, this could explain the excellent retention of over 4×10^4 s (Figure 4d) while it also provides an explanation for the asymmetric behavior in the *I*–*V* curves when the polarity is switched. During sweeping to negative potentials (with ITO grounded), the Na^+ ions diffuse toward the Ag electrode. It has been reported that sodium diffusion, which results in Na^+ deficiency in the HE-PBA, and an applied potential, leading to an electric field over the device, can result in a change of conductivity, which hints at a bulk reaction of the HE-PBA layer rather than formation of conducting filaments (as is the case for many filamentary memristive devices).[5] When sweeping back to positive potentials, the Na^+ ions reinsert into the HE-PBA, which is reflected in a similar *I*–*V* curve to the initial state (Figure 5e,i).

Table 1. Reaction enthalpies computed using DFT. ΔH_1 and ΔH_2 represent the reaction enthalpies calculated using Equations 1 and 2. The mean voltage is calculated by $\bar{V} = \frac{\Delta H}{(x_1 - x_2)F}$, where F is the Faraday constant.

x_1	x_2	ΔH_1 [kJ/mol]	$\bar{V}_1$ [V]	ΔH_2 [kJ/mol]	$\bar{V}_2$ [V]
1.3750	1.3125	13.17	2.18	3.29	0.54
1.3125	1.2500	14.12	2.34	4.24	0.70
1.2500	1.0000	57.47	2.38	17.95	0.74

As mentioned above, it is assumed that upon applying a bias voltage of −0.4 V, the Na^+ ions migrate toward the Ag electrode and the system becomes conductive. For more detailed insights into the mechanism, DFT calculations of the HE-PBA with different sodium concentrations were performed. By using DFT to determine the reaction enthalpy (ΔH) associated with the changes of HE-PBA during the SET and RESET process, the Na content (x) at the given potentials was found to be between 1.375 and 1.0. This was computed based on the following chemical reaction:

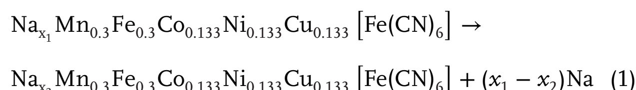

$$\mathrm{Na}_{x_1}\mathrm{Mn}_{0.3}\mathrm{Fe}_{0.3}\mathrm{Co}_{0.133}\mathrm{Ni}_{0.133}\mathrm{Cu}_{0.133}\left[\mathrm{Fe(CN)}_6\right] \rightarrow \mathrm{Na}_{x_2}\mathrm{Mn}_{0.3}\mathrm{Fe}_{0.3}\mathrm{Co}_{0.133}\mathrm{Ni}_{0.133}\mathrm{Cu}_{0.133}\left[\mathrm{Fe(CN)}_6\right] + (x_1 - x_2)\mathrm{Na} \quad (1)$$

In this equation, x_1 represents the initial number of sodium ions within the lattice, while x_2 denotes that remaining in the lattice after the reaction. The difference ($x_1 - x_2$) corresponds to the number of ions released from the lattice forming sodium metal. The results shown in **Table 1** reveal that the reaction enthalpies (ΔH_1) for the complete Na removal process are significant across all examined concentrations, yielding a mean voltage $\bar{V}_1$ (2.3 V) much higher than the experimental average resistive switching voltage of V_{SET} (−0.26 V) and V_{RESET} (0.36 V). Nevertheless, the considered reaction represents an extreme scenario, in which Na is fully removed from the HE-PBA and forms sodium metal. The smaller obtained V_{SET} compared to the mean voltage derived from the DFT calculations suggests that sodium is not entirely extracted from the HE-PBA during the experiment. Rather, we hypothesize that they begin diffusing toward the Ag electrode under the influence of applied electric field, adsorbing at the Ag|HE-PBA interface. The reaction enthalpy (ΔH_2) for such a process is calculated considering the following reaction:

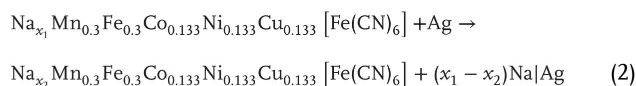

$$\mathrm{Na}_{x_1}\mathrm{Mn}_{0.3}\mathrm{Fe}_{0.3}\mathrm{Co}_{0.133}\mathrm{Ni}_{0.133}\mathrm{Cu}_{0.133}\left[\mathrm{Fe(CN)}_6\right] + \mathrm{Ag} \rightarrow \mathrm{Na}_{x_2}\mathrm{Mn}_{0.3}\mathrm{Fe}_{0.3}\mathrm{Co}_{0.133}\mathrm{Ni}_{0.133}\mathrm{Cu}_{0.133}\left[\mathrm{Fe(CN)}_6\right] + (x_1 - x_2)\mathrm{Na|Ag} \quad (2)$$

where an Ag metal surface was used and reaction between Na and Ag was allowed (denoted as Na|Ag). Employing a suitable

© 2024 The Author(s). Advanced Materials published by Wiley-VCH GmbH

15214095, 0, Downloaded from https://onlinelibrary.wiley.com/doi/10.1002/adma.202410060 by Karlsruher Institut F., Wiley Online Library on [08/12/2024]. See the Terms and Conditions (https://onlinelibrary.wiley.com/terms-and-conditions) on Wiley Online Library for rules of use; OA articles are governed by the applicable Creative Commons License

15214095, 0, Downloaded from https://onlinelibrary.wiley.com/doi/10.1002/adma.202410060 by Karlsruher Institut F., Wiley Online Library on [08/12/2024]. See the Terms and Conditions (https://onlinelibrary.wiley.com/terms-and-conditions) on Wiley Online Library for rules of use; OA articles are governed by the applicable Creative Commons License

methodology,[83] we calculated the Na adsorption onto the (100), (110), and (111) crystal planes of silver metal, taking the average binding energies into account. As indicated in Table 1, after accounting for the binding, the reaction enthalpy significantly decreased, with the average voltage $\bar{V}_2$ (0.66 V) aligning more closely with the experimental V_{SET} and V_{RESET} values. The slight discrepancy between the theoretical predictions and the experimental results may be attributed to the limitations of the simplified model. Although the model attempts to represent Na adsorption onto the Ag electrode, it inherently simplifies the structure and interactions. Specifically, the model does not fully account for the complex and potentially infinite nature of the Ag crystal planes, nor does it comprehensively represent the complex Na-Ag interactions. These simplifications could be one of the main factors contributing to the observed differences.[83] Yet, the DFT results demonstrate that Na is not fully extracted from HE-PBA to form sodium metal. Instead, they likely bind at the interface with the Ag electrode, causing a bulk change in the HE-PBA. This in turn gives rise to low energy consumption and the non-volatile device character. Furthermore, the formation of a complex Na-Ag network at the interface has been demonstrated previously by molecular dynamics simulations.[83] In comparison to the findings by Nguyen et al.,[64] who demonstrated lithium migration from Li_xCoO_2 films into a silicon electrode in an RS device, our study provides an alternative mechanism, where sodium atoms are not fully extracted but rather diffuse and adsorb onto the Ag electrode.

Further DFT calculations were conducted to investigate the transition between the insulating and conducting states in the HE-PBA concentration range between 1.375 and 1.0. This particular region was chosen based on prior observations that Li_xCoO_2 undergoes a transition from ceramic to metallic state with a minor compositional change from $x = 1$ to 0.94.[84] In analogy, we hypothesized that HE-PBA would exhibit a similar behavior. Therefore, we focused on concentrations proximate to the compound's concentration, starting at x(Na) = 1.375 and extending toward lower concentrations. Figure S13 (Supporting Information) illustrates the respective crystal structures with $x = 1.375$, 1.3125, 1.25, and 1.0 in $Na_xM[Fe(CN)_6]$. Considering that variations in sodium content directly affect the electronic conductivity of the Ag/HE-PBA/ITO device, we examined the electronic structure of HE-PBA by calculating the total and projected density of states (pDOS).

The results are shown in **Figure 6a–d**. At x(Na) = 1.3125, minor states associated with Co and C-coordinated Fe (Fe_1) begin to overlap with the Fermi energy level, as detailed in the zoomed-in view of Figure 6b. This overlap increases the density of states at the Fermi level, enhancing the number of available charge carriers. As electrons can be readily excited to these states at room temperature, they behave as free electrons that can move within the material, thus increasing the electrical conductivity. The general electronic system and the density of states that are assigned to each element in Figure 6b are a result of the interactions of the different elements incorporated in the HEM. These so-called cocktail effects seem to have a big influence on the electronic band structure, enabling the superposition of the Fe_1 and Co states to render the material conductive. This effect is more pronounced at x(Na) = 1.25, where the density of states increases more at and around the Fermi level, indicating a transition to a metallic-like state. Consequently, an enhancement in electrical conductivity is anticipated. With further decrease in sodium content, the DOS at the Fermi energy level increases rapidly, indicating a stronger metallic character. This slight change in sodium concentration appears to be sufficient to alter the electrical properties.[64] The same phenomenon has been observed, for example in Li_xCoO_2, where studies show a nonmetal-metal transition with decreasing lithium content.[84–86]

In short, the DFT results indicate that the Ag/HE-PBA/ITO device utilizes the low energy process of sodium extraction/insertion coordinated with the Ag electrode while maintaining non-volatile resistance switching caused by an insulating-metallic transition with decreasing sodium concentration, which agrees reasonably well with the experimental data presented here.

To rule out any influence of Ag metal filaments on the RS behavior of the HE-PBA-based memristor, alternative inert TEs such as Pt and Au were tested as replacements for Ag. However, using deionized water-based Pt ink caused solvent incompatibility, leading to a hole in the HE-PBA film (Figure S14, Supporting Information).[87] Additionally, Au ink requires a curing temperature above 200 °C, causing structural degradation of HE-PBA.[88] To address this, ≈100 nm of Au was sputtered onto the surface of the HE-PBA layer (**Figure 7a**). Due to difficulties in precisely controlling the sputtering area, a large HE-PBA film was prepared and tape was used to isolate the Au deposition. Despite these challenges, the device exhibits self-compliance behavior, regardless of whether positive or negative voltages are applied to the Au electrode (Figure 7b). Given the relatively high self-compliance of ≈4 mA observed with the sputtered TE, an external CC of 0.3 mA was applied to minimize power consumption and protect the device. The Au/HE-PBA/ITO device exhibited a switching voltage of ≈1.5 V, with continuous switching behavior over 30 cycles and an $R_{\mathrm{OFF}}/R_{\mathrm{ON}}$ ratio exceeding 10^2 (Figure 7c,d). These results indicate that Ag metal filaments are less likely responsible for the memristive behavior, as the device functions effectively without using Ag as TE (Figure 7e); the negative voltage applied in the case of Ag/HE-PBA/ITO device does not result in the formation of Ag filaments, as the electric field is directed from the ITO to the Ag electrode. While it cannot be completely ruled out that the Ag filaments might accumulate during the RESET process when a positive voltage is applied, which may impact device performance, this risk even persists at low applied voltages (0.5 V) during pulsed operation. However, the formation of conducting filaments, growing from the ITO to the Ag electrode, is unlikely at such a low positive voltage, as this process typically requires much higher electroforming voltages, often exceeding 1 V or even several volts.[89] This is further supported by Table S5 (Supporting Information), which provides a comparison of electroforming voltages for various memristors. Additionally, the movement of vacancies in MOFs is either not feasible or can be considered equiv. to the proposed mechanism, since either ions or vacancies/holes are involved. This mechanism is also supported by literature studies,[64,90] where insertion materials were used to fabricate memristors with a mechanism similar to the one presented here. The high-entropy MOF employed in the present work can function as an insertion-type electrode (facilitating Na^+ transport), making the mechanism likely analogous to the one previously reported.

 © 2024 The Author(s). Advanced Materials published by Wiley-VCH GmbH

15214095, 0, Downloaded from https://onlinelibrary.wiley.com/doi/10.1002/adma.202410060 by Karlsruher Institut F., Wiley Online Library on [08/12/2024]. See the Terms and Conditions (https://onlinelibrary.wiley.com/terms-and-conditions) on Wiley Online Library for rules of use; OA articles are governed by the applicable Creative Commons License

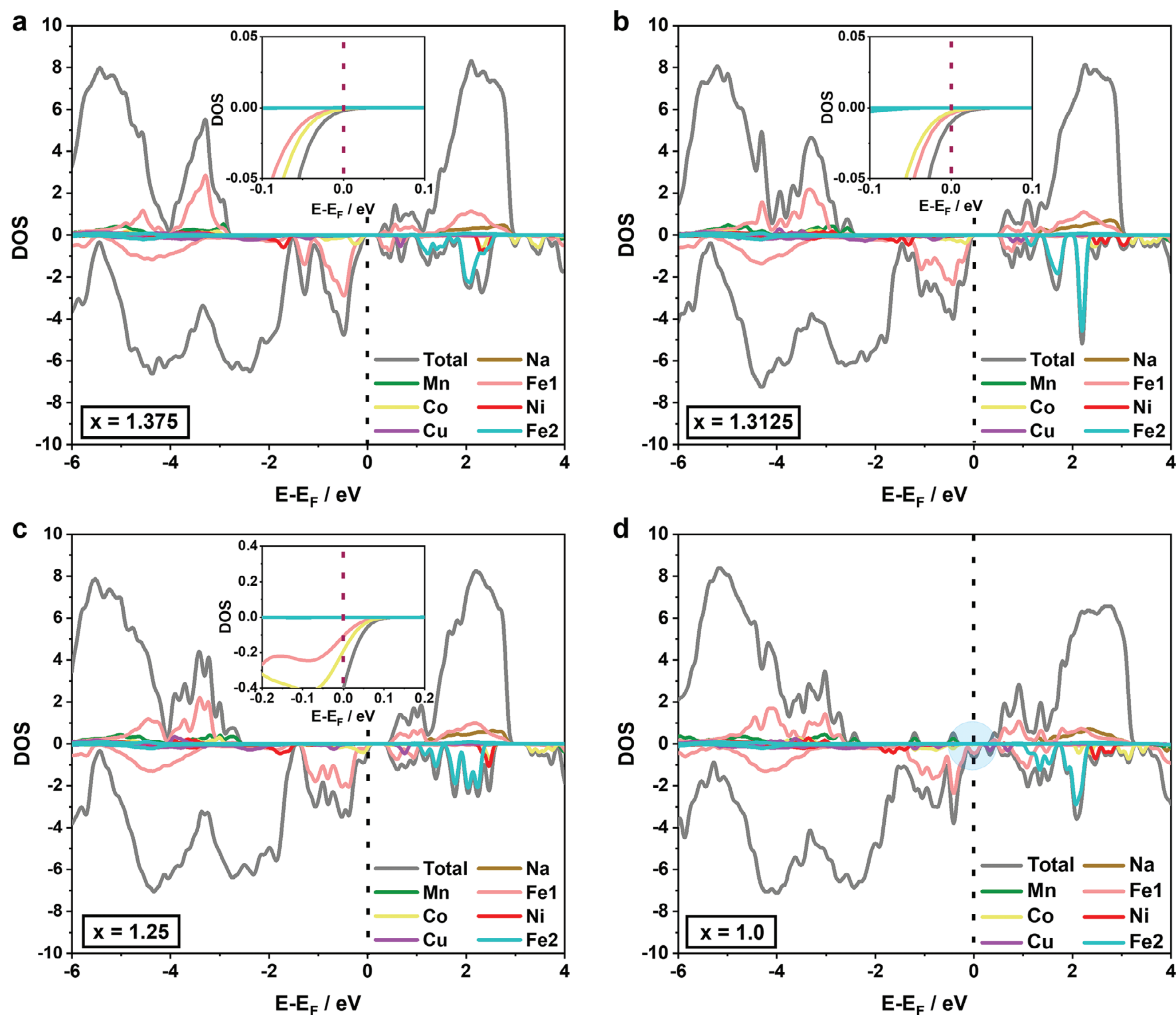

Figure 6. Total and projected DOS of $Na_xM[Fe(CN)_6]$ with a) $x = 1.375$, b) $x = 1.3125$, c) $x = 1.25$, and d) $x = 1.0$, with the Fermi energy shift to 0. Panels (a), (b), and (c) include zoomed-in views of the DOS near the Fermi energy. Fe_1 and Fe_2 denote the C- and N-coordinated Fe, respectively.

Overall, the device shows promising non-volatile resistive switching performance. However, further improvements are necessary, as discussed here. Based on the endurance (Figure S10, Supporting Information; Figure 4a), it is evident that the LRS is more stable with less fluctuation, suggesting that Na^+ extraction is relatively easier while the insertion process is more difficult. Several factors can influence this, including the structural properties of active layer (thickness, morphology, intrinsic defects), ion mobility (kinetics), or potential accumulation of Ag metal filaments. The thickness and quality of the active layer are critical for ensuring stable HRS and LRS, as noted in other studies.[77] In the current work, the HE-PBA particle size, ranging from 100 to 300 nm, presents challenges in forming dense films and achieving precise control over layer thickness. A thicker film may hinder ion transport, leading to fluctuations in the HRS and LRS. Improving the HE-PBA-based device's performance by reducing fluctuations between HRS and LRS while maintaining low power consumption through optimized applied voltages and active layer thickness is feasible, as shown in Figure S15 (Supporting Information). Yet, further improvements in cycling stability are required for practical applications. In-depth exploration of alternative electrodes may provide opportunities to increase the device's long-term stability.

In summary, this work proposes that Na^+ ion transport drives the resistive switching—rather than relying on the formation/rupture of Ag conducting filaments—making the HE-PBA-based device a promising candidate for low-power, non-volatile memory applications.

© 2024 The Author(s). Advanced Materials published by Wiley-VCH GmbH

15214095, 0, Downloaded from https://onlinelibrary.wiley.com/doi/10.1002/adma.202410060 by Karlsruher Institut F., Wiley Online Library on [08/12/2024]. See the Terms and Conditions (https://onlinelibrary.wiley.com/terms-and-conditions) on Wiley Online Library for rules of use; OA articles are governed by the applicable Creative Commons License

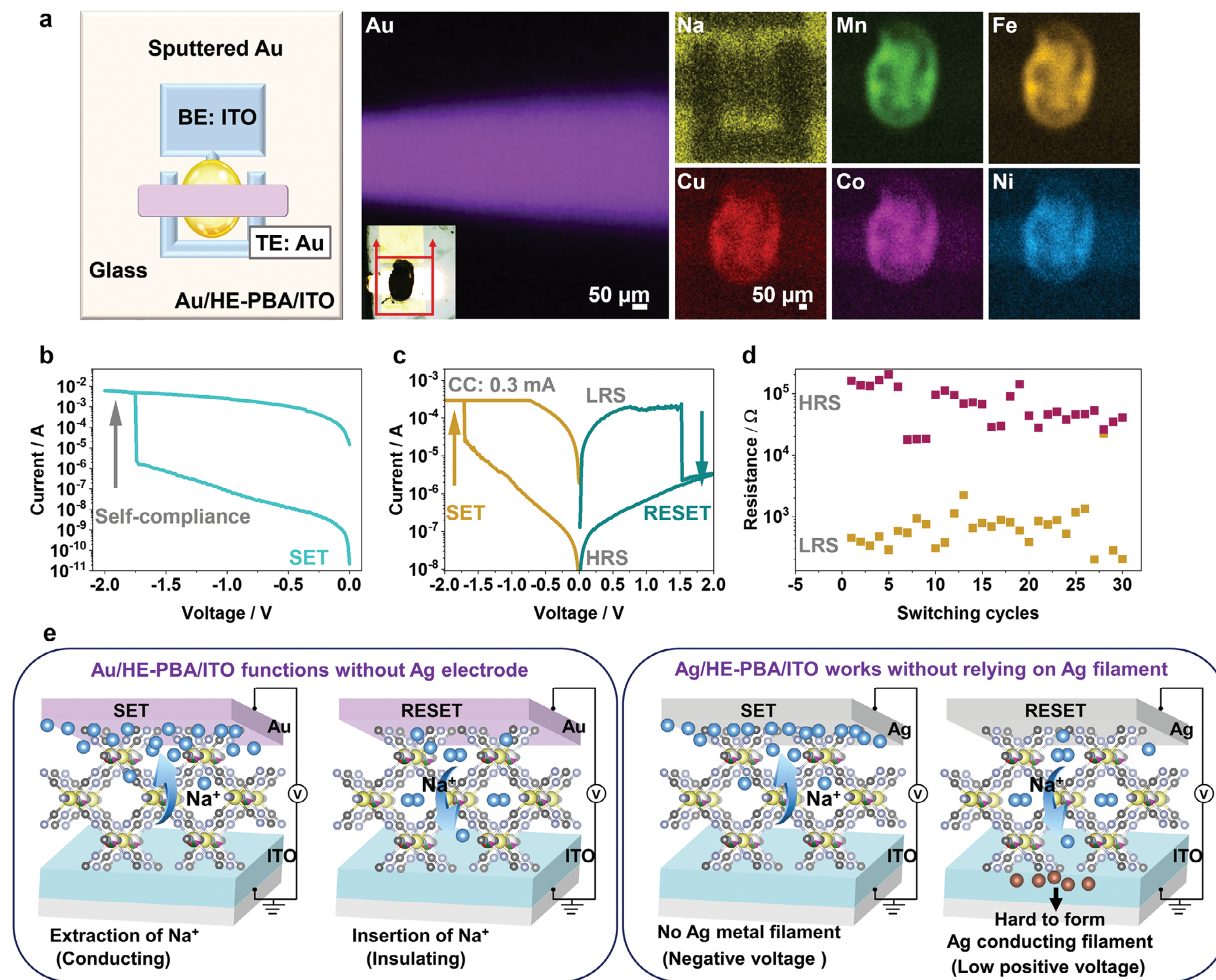

Figure 7. a) Schematic and elemental distribution of the Au/HE-PBA/ITO device with sputtered Au as TE. Electric characterization of the device: b) Self-compliance behavior, c) initial *I–V* curves, and d) endurance over 30 sweeping cycles. e) Corresponding schematic representations of the resistive switching mechanism.

3. Conclusions

In this study, we introduce a Na^+-modulated, non-volatile, printed memristor of structure/composition Ag/$Na_{1.38}Mn_{0.3}Fe_{0.3}Ni_{0.133}Cu_{0.133}Co_{0.133}[Fe(CN)_6]_{0.84}\square_{0.16}\cdot 0.92H_2O$ (HE-PBA)/ITO. This memristor demonstrates major advantages such as low power consumption, self-compliance, and forming-free behavior in memory applications. Also, the Ag/HE-PBA/ITO device exhibits metallic behavior in the low resistance state and insulating behavior in the high resistance state. Through comprehensive experiments and simulation studies, we elucidate that the insulating-metallic transition arises from the extraction/insertion of Na^+ ions, rather than the formation/rupture of Ag conducting filaments. Leveraging the low-energy process of ion (de)insertion coupled with the Ag electrode, the Ag/HE-PBA/ITO device displays robust retention stability and high R_{OFF}/R_{ON} ratio as a non-volatile memristor. Notably, the ion-driven resistive switching strategy presented in our study may provide new insights for addressing the high power consumption and volatile storage problems encountered in other insertion-type memristors.

Supporting Information

Supporting Information is available from the Wiley Online Library or from the author.

Acknowledgements

Y.H. and Y.D. acknowledge financial support from the China Scholarship Council (CSC). The authors further acknowledge the support from the Karlsruhe Nano Micro Facility (KNMFi, www.knmf.kit.edu), a Helmholtz research infrastructure at Karlsruhe Institute of Technology (KIT, www.kit.edu). J.L. acknowledges the Fonds der Chemischen Industrie (FCI) for financial support. Y.T. and P.K. acknowledge the provision of computational resources by the Jülich Aachen Research Alliance-Center for Simulation and Data Science (JARA-CSD, project no. cjiek61). J.A.-H. and

© 2024 The Author(s). Advanced Materials published by Wiley-VCH GmbH

H.H. acknowledge funding by the DFG under Germany's Excellence Strategy via the Excellence Cluster "3D Matter Made to Order" (EXC-2082/1-390761711) as well as the Carl Zeiss Foundation. J.A.-H., S.S., and B.B. are grateful for financial support from the KIT via the project Auto.MAP and the Helmholtz Program "Materials Systems Engineering" under program no. 43.31.01. The authors further thank Bastian Weinert for assistance with the µXRF measurements.

Open access funding enabled and organized by Projekt DEAL.

Conflict of Interest

The authors declare no conflict of interest.

Author Contributions

Y.H. conceived the idea, designed the experiments, conducted most of the characterizations, analyzed the results, and drafted the manuscript. J.A.-H. and B.B. supervised the work and provided the main comments on the manuscript. T.B. corrected the manuscript. Y.T. and P.K. performed the DFT calculations. H.-R.H. assisted in electrical characterizations and analyses. T.D. contributed to the XPS analyses. Y.D. assisted in the TEM measurements. J.L. assisted in the DSC measurements. S.S. and G.M. assisted with the physical characterizations. Y.M. assisted in the ICP-OES analysis. J.A.-H. provided the research funding and H.H. provided the first year funding. All authors commented on the manuscript.

Data Availability Statement

The data that support the findings of this study are available from the corresponding author upon reasonable request.

Keywords

high-entropy PBA, memristors, non-volatile memory, resistive switching mechanism

Received: July 12, 2024
Revised: October 13, 2024
Published online:

[1] Y. Liu, X. Li, H. Zheng, N. Chen, X. Wang, X. Zhang, H. Sun, S. Zhang, *Adv. Funct. Mater.* **2021**, *31*, 2009803.
[2] S. Han, Y. Zhou, V. A. L. Roy, *Adv. Mater.* **2013**, *25*, 5425.
[3] M. Song, J. Kang, X. Zhang, W. Ji, A. Ascoli, I. Messaris, A. S. Demirkol, B. Dong, S. Aggarwal, W. Wan, S. Hong, S. G. Cardwell, I. Boybat, J. Seo, J. Lee, M. Lanza, H. Yeon, M. Onen, J. Li, B. Yildiz, J. A. del Alamo, S. Kim, S. Choi, G. Milano, C. Ricciardi, L. Alff, Y. Chai, Z. Wang, H. Bhaskaran, M. C. Hersam, et al., *ACS Nano* **2023**, *17*, 11994.
[4] K. Zhu, S. Pazos, F. Aguirre, Y. Shen, Y. Yuan, W. Zheng, O. Alharbi, M. A. Villena, B. Fang, X. Li, A. Milozzi, M. Farronato, M. Muñoz-Rojo, T. Wang, R. Li, H. Fariborzi, J. B. Roldan, G. Benstetter, X. Zhang, H. N. Alshareef, T. Grasser, H. Wu, D. Ielmini, M. Lanza, *Nature* **2023**, *618*, 57.
[5] G. Zhang, J. Qin, Y. Zhang, G. Gong, Z. Xiong, X. Ma, Z. Lv, Y. Zhou, S. Han, *Adv. Funct. Mater.* **2023**, *33*, 2302929.
[6] J. C. Gonzalez-Rosillo, M. Balaish, Z. D. Hood, N. Nadkarni, D. Fraggedakis, K. J. Kim, K. M. Mullin, R. Pfenninger, M. Z. Bazant, J. L. M. Rupp, *Adv. Mater.* **2020**, *32*, 1907465.
[7] C. Zhang, M. Chen, Y. Pan, Y. Li, K. Wang, J. Yuan, Y. Sun, Q. Zhang, *Adv. Sci.* **2023**, *10*, 2207229.
[8] Y. Huang, Y. Gu, S. Mohan, A. Dolocan, N. D. Ignacio, S. Kutagulla, K. Matthews, A. Londoño-Calderon, Y. Chang, Y. Chen, J. H. Warner, M. T. Pettes, J. C. Lee, D. Akinwande, *Adv. Funct. Mater.* **2023**, *34*, 2214250.
[9] Y. van de Burgt, E. Lubberman, E. J. Fuller, S. T. Keene, G. C. Faria, S. Agarwal, M. J. Marinella, A. Alec Talin, A. Salleo, *Nat. Mater.* **2017**, *16*, 414.
[10] A. Sebastian, M. Le Gallo, R. Khaddam-Aljameh, E. Eleftheriou, *Nat. Nanotechnol.* **2020**, *15*, 529.
[11] Y. Lin, F. Meng, T. Zeng, Q. Zhang, Z. Wang, Y. Cheng, X. Zhao, L. Gu, H. Xu, Y. Liu, *Adv. Funct. Mater.* **2023**, *33*, 2302787.
[12] R. Marquardt, F. Zahari, J. Carstensen, G. Popkirov, O. Gronenberg, G. Kolhatkar, H. Kohlstedt, M. Ziegler, *Adv. Electron. Mater.* **2023**, *9*, 2201227.
[13] E. Carlos, R. Branquinho, R. Martins, A. Kiazadeh, E. Fortunato, *Adv. Mater.* **2021**, *33*, 2004328.
[14] Y. Abbas, S. M. Ansari, I. Taha, H. Abunahla, M. U. Khan, M. Rezeq, H. M. Aldosari, B. Mohammad, *Adv. Funct. Mater.* **2024**, *34*, 2214615.
[15] M. D. Tran, H. Kim, J. S. Kim, M. H. Doan, T. K. Chau, Q. A. Vu, J. Kim, Y. H. Lee, *Adv. Mater.* **2019**, *31*, 1807075.
[16] S. Batool, M. Idrees, S.-R. Zhang, S.-T. Han, Y. Zhou, *Nanoscale Horiz.* **2022**, *7*, 480.
[17] S. P. Rath, D. Thompson, S. Goswami, S. Goswami, *Adv. Mater.* **2023**, *35*, 2204551.
[18] E. J. Yoo, M. Lyu, J.-H. Yun, C. J. Kang, Y. J. Choi, L. Wang, *Adv. Mater.* **2015**, *27*, 6170.
[19] J. H. Heo, D. H. Shin, S. H. Moon, M. H. Lee, D. H. Kim, S. H. Oh, W. Jo, S. H. Im, *Sci. Rep.* **2017**, *7*, 16586.
[20] Y. Lin, X. Zhang, X. Shan, T. Zeng, X. Zhao, Z. Wang, Z. Kang, H. Xu, Y. Liu, *J. Mater. Chem. C* **2020**, *8*, 14789.
[21] C. Li, L. Han, H. Jiang, M.-H. Jang, P. Lin, Q. Wu, M. Barnell, J. J. Yang, H. L. Xin, Q. Xia, *Nat. Commun.* **2017**, *8*, 15666.
[22] H. Yeon, P. Lin, C. Choi, S. H. Tan, Y. Park, D. Lee, J. Lee, F. Xu, B. Gao, H. Wu, H. Qian, Y. Nie, S. Kim, J. Kim, *Nat. Nanotechnol.* **2020**, *15*, 574.
[23] C. Chen, Y. C. Yang, F. Zeng, F. Pan, *Appl. Phys. Lett.* **2010**, *97*, 083502.
[24] H.-D. Kim, H.-M. An, S. M. Hong, T. G. Kim, *Phys. status solidi (a)* **2013**, *210*, 1822.
[25] X. Zhao, Z. Wang, Y. Xie, H. Xu, J. Zhu, X. Zhang, W. Liu, G. Yang, J. Ma, Y. Liu, *Small* **2018**, *14*, 1801325.
[26] A. Sood, A. D. Poletayev, D. A. Cogswell, P. M. Csernica, J. T. Mefford, D. Fraggedakis, M. F. Toney, A. M. Lindenberg, M. Z. Bazant, W. C. Chueh, *Nat. Rev. Mater.* **2021**, *6*, 847.
[27] A. Amiri, R. Shahbazian-Yassar, *J. Mater. Chem. A* **2021**, *9*, 782.
[28] Y. Ma, Y. Ma, Q. Wang, S. Schweidler, M. Botros, T. Fu, H. Hahn, T. Brezesinski, B. Breitung, *Energy Environ. Sci.* **2021**, *14*, 2883.
[29] E. P. George, D. Raabe, R. O. Ritchie, *Nat. Rev. Mater.* **2019**, *4*, 515.
[30] M. C. Gao, D. B. Miracle, D. Maurice, X. Yan, Y. Zhang, J. A. Hawk, *J. Mater. Res.* **2018**, *33*, 3138.
[31] X. Shi, J. Zou, Z. Chen, *Chem. Rev.* **2020**, *120*, 7399.
[32] Y. Yao, Q. Dong, A. Brozena, J. Luo, J. Miao, M. Chi, C. Wang, I. G. Kevrekidis, Z. J. Ren, J. Greeley, G. Wang, A. Anapolsky, L. Hu, *Science* **2022**, *376*, eabn3103.
[33] W. Xu, H. Chen, K. Jie, Z. Yang, T. Li, S. Dai, *Angew. Chem., Int. Ed.* **2019**, *58*, 5018.
[34] T. A. A. Batchelor, J. K. Pedersen, S. H. Winther, I. E. Castelli, K. W. Jacobsen, J. Rossmeisl, *Joule* **2019**, *3*, 834.
[35] Y. He, S. L. Dreyer, Y. Ting, Y. Ma, Y. Hu, D. Goonetilleke, Y. Tang, T. Diemant, B. Zhou, P. M. Kowalski, M. Fichtner, H. Hahn, J. Aghassi-Hagmann, T. Brezesinski, B. Breitung, Y. Ma, *Angew. Chem.* **2024**, *136*, e202315371.

© 2024 The Author(s). Advanced Materials published by Wiley-VCH GmbH

15214095, 0, Downloaded from https://onlinelibrary.wiley.com/doi/10.1002/adma.202410060 by Karlsruher Institut F., Wiley Online Library on [08/12/2024]. See the Terms and Conditions (https://onlinelibrary.wiley.com/terms-and-conditions) on Wiley Online Library for rules of use; OA articles are governed by the applicable Creative Commons License

[36] Y. Ma, Y. Hu, Y. Pramudya, T. Diemant, Q. Wang, D. Goonetilleke, Y. Tang, B. Zhou, H. Hahn, W. Wenzel, M. Fichtner, Y. Ma, B. Breitung, T. Brezesinski, *Adv. Funct. Mater.* **2022**, *32*, 2202372.
[37] Y. Ma, Y. Ma, S. L. Dreyer, Q. Wang, K. Wang, D. Goonetilleke, A. Omar, D. Mikhailova, H. Hahn, B. Breitung, T. Brezesinski, *Adv. Mater.* **2021**, *33*, 2101342.
[38] Y. He, S. L. Dreyer, T. Akçay, T. Diemant, R. Mönig, Y. Ma, Y. Tang, H. Wang, J. Lin, S. Schweidler, M. Fichtner, H. Hahn, T. Brezesinski, B. Breitung, Y. Ma, *ACS Nano* **2024**, *18*, 24441.
[39] H. Yi, R. Qin, S. Ding, Y. Wang, S. Li, Q. Zhao, F. Pan, *Adv. Funct. Mater.* **2021**, *31*, 2006970.
[40] J. Qian, C. Wu, Y. Cao, Z. Ma, Y. Huang, X. Ai, H. Yang, *Adv. Energy Mater.* **2018**, *8*, 1702619.
[41] K. Hurlbutt, S. Wheeler, I. Capone, M. Pasta, *Joule* **2018**, *2*, 1950.
[42] T. Shibata, Y. Moritomo, *Chem. Commun.* **2014**, *50*, 12941.
[43] M. Takachi, Y. Fukuzumi, Y. Moritomo, *Dalton Trans.* **2016**, *45*, 458.
[44] D. A. Robinson, M. E. Foster, C. H. Bennett, A. Bhandarkar, E. R. Webster, A. Celebi, N. Celebi, E. J. Fuller, V. Stavila, C. D. Spataru, D. S. Ashby, M. J. Marinella, R. Krishnakumar, M. D. Allendorf, A. A. Talin, *Adv. Mater.* **2023**, *35*, 2207595.
[45] K. Yan, J. Li, L. Pan, Y. Shi, *APL Mater.* **2020**, *8*, 120705.
[46] H. Hu, A. Scholz, Y. Liu, Y. Tang, G. C. Marques, J. Aghassi-Hagmann, *IEEE Trans. Electron Devices* **2023**, *70*, 3051.
[47] H. Zhang, X. Ju, Y. Zhou, C. Gu, J. Pan, D. S. Ang, *ACS Appl. Mater. Interfaces* **2019**, *11*, 41490.
[48] G. Ding, Y. Wang, G. Zhang, K. Zhou, K. Zeng, Z. Li, Y. Zhou, C. Zhang, X. Chen, S. T. Han, *Adv. Funct. Mater.* **2019**, *29*, 1806637.
[49] N. C Branca, J. Deuermeier, J. Martins, E. Carlos, M. Pereira, R. Martins, E. Fortunato, A. Kiazadeh, *Adv. Electron. Mater.* **2020**, *6*, 1900958.
[50] M. Ahn, Y. Park, S. H. Lee, S. Chae, J. Lee, J. T. Heron, E. Kioupakis, W. D. Lu, J. D. Phillips, *Adv. Electron. Mater.* **2021**, *7*, 2001258.
[51] B. S. Murty, J.-W. Yeh, R. Srikanth, P. P. Bhattacharjee, *High-Entropy Alloys*, Elsevier, **2019**.
[52] J. C. Pramudita, S. Schmid, T. Godfrey, T. Whittle, M. Alam, T. Hanley, H. E. A. Brand, N. Sharma, *Phys. Chem. Chem. Phys.* **2014**, *16*, 24178.
[53] Y. Tang, W. Li, P. Feng, M. Zhou, K. Wang, Y. Wang, K. Zaghib, K. Jiang, *Adv. Funct. Mater.* **2020**, *30*, 1908754.
[54] F. L. Faita, L. B. Avila, J. P. B. Silva, M. H. Boratto, C. C. P. Cid, C. F. O. Graeff, M. J. M. Gomes, C. K. Müller, A. A. Pasa, *J. Alloys Compd.* **2022**, *896*, 162971.
[55] Y. You, X. Yu, Y. Yin, K.-W. Nam, Y.-G. Guo, *Nano Res.* **2015**, *8*, 117.
[56] L. Samain, B. Gilbert, F. Grandjean, G. J. Long, D. Strivay, *J. Anal. At. Spectrom.* **2013**, *28*, 524.
[57] Y. You, X. Wu, Y. Yin, Y. Guo, *Energy Environ. Sci.* **2014**, *7*, 1643.
[58] Y. Liu, D. He, R. Han, G. Wei, Y. Qiao, *Chem. Commun.* **2017**, *53*, 5569.
[59] Y. Huang, M. Xie, J. Zhang, Z. Wang, Y. Jiang, G. Xiao, S. Li, L. Li, F. Wu, R. Chen, *Nano Energy* **2017**, *39*, 273.
[60] I. Sarhid, I. Lampre, D. Dragoe, P. Beaunier, B. Palpant, H. Remita, *Materials* **2019**, *12*, 3012.
[61] Q. Wang, A. Sarkar, D. Wang, L. Velasco, R. Azmi, S. S. Bhattacharya, T. Bergfeldt, A. Düvel, P. Heitjans, T. Brezesinski, H. Hahn, B. Breitung, *Energy Environ. Sci.* **2019**, *12*, 2433.
[62] X. Zhang, M. Xia, T. Liu, N. Peng, H. Yu, R. Zheng, L. Zhang, M. Shui, J. Shu, *Chem. Eng. J.* **2021**, *421*, 127767.
[63] M. C. Biesinger, B. P. Payne, A. P. Grosvenor, L. W. M. Lau, A. R. Gerson, R. S. C. Smart, *Appl. Surf. Sci.* **2011**, *257*, 2717.
[64] V. S. Nguyen, V. H. Mai, P. Auban Senzier, C. Pasquier, K. Wang, M. J. Rozenberg, N. Brun, K. March, F. Jomard, J. Giapintzakis, C. N. Mihailescu, E. Kyriakides, P. Nukala, T. Maroutian, G. Agnus, P. Lecoeur, S. Matzen, P. Aubert, S. Franger, R. Salot, P.-A. Albouy, D. Alamarguy, B. Dkhil, P. Chrétien, O. Schneegans, *Small* **2018**, *14*, 1801038.
[65] R. Waser, R. Dittmann, G. Staikov, K. Szot, *Adv. Mater.* **2009**, *21*, 2632.
[66] R. Waser, M. Aono, *Nat. Mater.* **2007**, *6*, 833.
[67] M. K. Kim, J. S. Lee, *ACS Appl. Mater. Interfaces* **2016**, *8*, 32918.
[68] Q. Hu, R. Li, X. Zhang, Q. Gao, M. Wang, H. Shi, Z. Xiao, P. K. Chu, A. Huang, *Sci. Rep.* **2019**, *9*, 5081.
[69] X. Zhu, C. S. Ong, X. Xu, B. Hu, J. Shang, H. Yang, S. Katlakunta, Y. Liu, X. Chen, L. Pan, J. Ding, R.-W. Li, *Sci. Rep.* **2013**, *3*, 1084.
[70] T.-H. Hou, K.-L. Lin, J. Shieh, J.-H. Lin, C.-T. Chou, Y.-J. Lee, *Appl. Phys. Lett.* **2011**, *98*, 103511.
[71] C. Ye, C. Zhan, T.-M. Tsai, K.-C. Chang, M.-C. Chen, T.-C. Chang, T. Deng, H. Wang, *Appl. Phys. Express* **2014**, *7*, 034101.
[72] C. B. Lee, D. S. Lee, A. Benayad, S. R. Lee, M. Chang, M.-J. Lee, J. Hur, Y. B. Kim, C. J. Kim, U.-I. Chung, *IEEE Electron Device Lett.* **2011**, *32*, 399.
[73] G. W. Burr, R. M. Shelby, A. Sebastian, S. Kim, S. Kim, S. Sidler, K. Virwani, M. Ishii, P. Narayanan, A. Fumarola, L. L. Sanches, I. Boybat, M. Le Gallo, K. Moon, J. Woo, H. Hwang, Y. Leblebici, *Adv. Phys. X* **2017**, *2*, 89.
[74] L. B. Avila, P. C. Serrano Arambulo, A. Dantas, E. E. Cuevas-Arizaca, D. Kumar, C. K. Müller, *Nanomaterials* **2022**, *12*, 2881.
[75] L. B. Avila, C. K. Müller, D. Hildebrand, F. L. Faita, B. F. Baggio, C. C. P. Cid, A. A. Pasa, *Materials* **2020**, *13*, 5618.
[76] F. Cai, J. M. Correll, S. H. Lee, Y. Lim, V. Bothra, Z. Zhang, M. P. Flynn, W. D. Lu, *Nat. Electron.* **2019**, *2*, 290.
[77] M. Lanza, R. Waser, D. Ielmini, J. J. Yang, L. Goux, J. Suñe, A. J. Kenyon, A. Mehonic, S. Spiga, V. Rana, S. Wiefels, S. Menzel, I. Valov, M. A. Villena, E. Miranda, X. Jing, F. Campabadal, M. B. Gonzalez, F. Aguirre, F. Palumbo, K. Zhu, J. B. Roldan, F. M. Puglisi, L. Larcher, T.-H. Hou, T. Prodromakis, Y. Yang, P. Huang, T. Wan, Y. Chai, et al., *ACS Nano* **2021**, *15*, 17214.
[78] F.-C. Chiu, *Adv. Mater. Sci. Eng.* **2014**, *2014*, 578168.
[79] C. A. Marianetti, G. Kotliar, G. Ceder, *Nat. Mater.* **2004**, *3*, 627.
[80] T. Motohashi, Y. Sugimoto, Y. Masubuchi, T. Sasagawa, W. Koshibae, T. Tohyama, H. Yamauchi, S. Kikkawa, *Phys. Rev. B* **2011**, *83*, 195128.
[81] Z. Wang, X. Zhang, S. Zhou, K. Edström, M. Strømme, L. Nyholm, *Adv. Funct. Mater.* **2018**, *28*, 1804038.
[82] N. Zhu, X. Mao, G. Wang, M. Zhu, H. Wang, G. Xu, M. Wu, H. K. Liu, S.-X. Dou, C. Wu, *J. Mater. Chem. A* **2021**, *9*, 13200.
[83] H. Wang, Y. Wu, S. Liu, Y. Jiang, D. Shen, T. Kang, Z. Tong, D. Wu, X. Li, C. Lee, *Small Methods* **2021**, *5*, 2001050.
[84] K. Kushida, K. Kuriyama, *Solid State Commun.* **2004**, *129*, 525.
[85] A. Milewska, K. Świerczek, J. Tobola, F. Boudoire, Y. Hu, D. K. Bora, B. S. Mun, A. Braun, J. Molenda, *Solid State Ionics* **2014**, *263*, 110.
[86] E. Flores, N. Mozhzhukhina, U. Aschauer, E. J. Berg, *ACS Appl. Mater. Interfaces* **2021**, *13*, 22540.
[87] M. Zea, A. Moya, M. Fritsch, E. Ramon, R. Villa, G. Gabriel, *ACS Appl. Mater. Interfaces* **2019**, *11*, 15160.
[88] W. Wang, Y. Gang, J. Peng, Z. Hu, Z. Yan, W. Lai, Y. Zhu, D. Appadoo, M. Ye, Y. Cao, Q. Gu, H. Liu, S. Dou, S. Chou, *Adv. Funct. Mater.* **2022**, *32*, 2111727.
[89] H. Hu, A. Scholz, C. Dolle, A. Zintler, A. Quintilla, Y. Liu, Y. Tang, B. Breitung, G. C. Marques, Y. M. Eggeler, J. Aghassi-Hagmann, *Adv. Funct. Mater.* **2024**, *34*, 2302290.
[90] X. Zhu, D. Li, X. Liang, W. D. Lu, *Nat. Mater.* **2019**, *18*, 141.

© 2024 The Author(s). Advanced Materials published by Wiley-VCH GmbH

15214095, 0, Downloaded from https://onlinelibrary.wiley.com/doi/10.1002/adma.202410060 by Karlsruher Institut F., Wiley Online Library on [08/12/2024]. See the Terms and Conditions (https://onlinelibrary.wiley.com/terms-and-conditions) on Wiley Online Library for rules of use; OA articles are governed by the applicable Creative Commons License